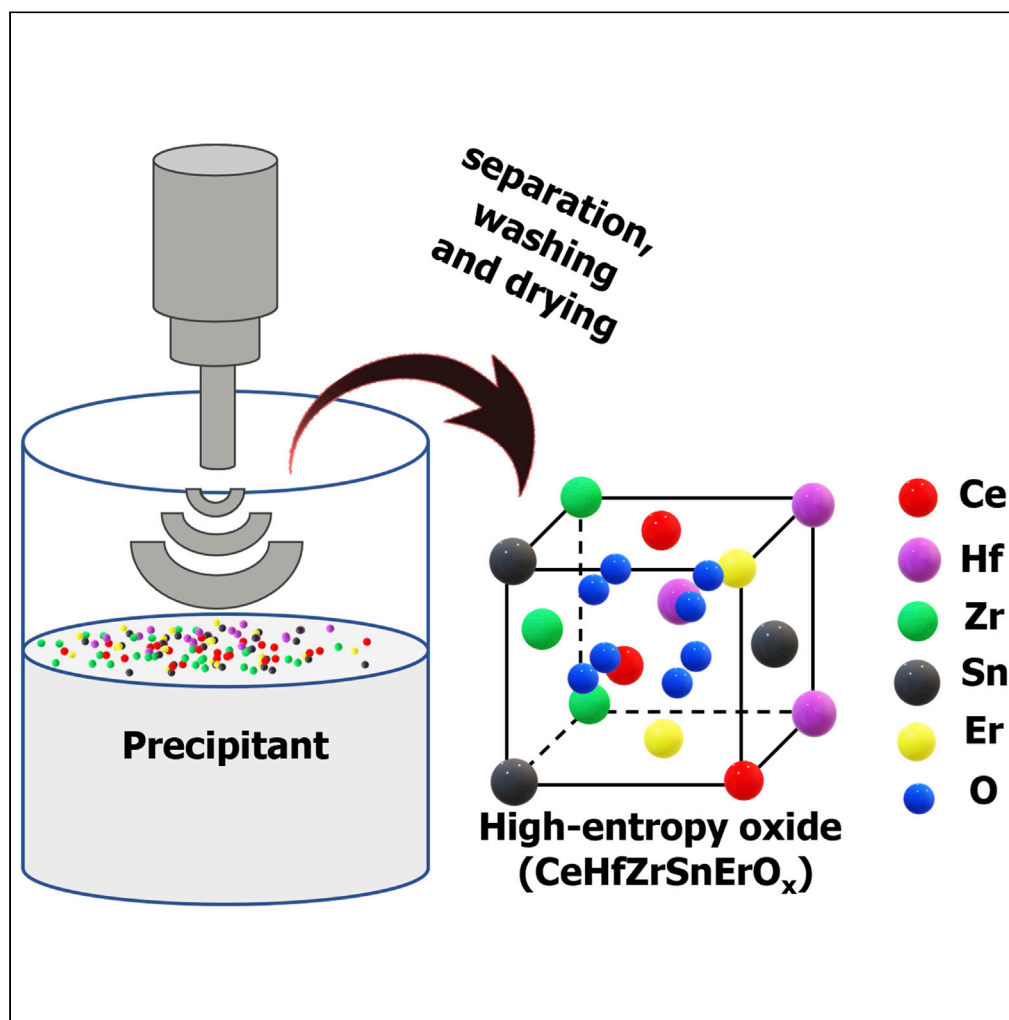## Article

Ultrasound-mediated synthesis of nanoporous fluorite-structured high-entropy oxides toward noble metal stabilization

Francis Okejiri,
Juntian Fan,
Zhennan Huang,
..., Felipe Polo-
Garzon, Zhenzhen
Yang, Sheng Dai

yangz3@ornl.gov (Z.Y.)
dais@ornl.gov (S.D.)

Highlights

Single-phase, fluorite-structured high-entropy oxides nanocrystals was synthesized

An ultrasound-mediated co-precipitation strategy under ambient conditions was used

$CeHfZrSnErO_x$ exhibited high surface area and high oxygen vacancy concentration

Pd nanoclusters within the $CeHfZrSnErO_x$ architecture can be stabilized

CellPress
OPEN ACCESS

Article

Ultrasound-mediated synthesis of nanoporous fluorite-structured high-entropy oxides toward noble metal stabilization

Francis Okejiri,[1,2] Juntian Fan,[1] Zhennan Huang,[3] Kevin Michael Siniard,[1] Miaofang Chi,[3] Felipe Polo-Garzon,[2] Zhenzhen Yang,[2,*] and Sheng Dai[1,2,4,*]

SUMMARY

High-entropy oxides (HEOs) are an emerging class of advanced ceramic materials capable of stabilizing ultrasmall nanoparticle catalysts. However, their fabrication still relies on high-temperature thermal treatment methodologies affording nonporous architectures. Herein, we report a facile synthesis of single-phase, fluorite-structured HEO nanocrystals via an ultrasound-mediated co-precipitation strategy under ambient conditions. Within 15 min of ultrasound exposure, high-quality fluorite-structured HEO ($CeHfZrSnErO_x$) was generated as ultrasmall-sized particles with high surface area and high oxygen vacancy concentration. Taking advantage of these unique structural features, palladium was introduced and stabilized in the form of highly dispersed Pd nanoclusters within the $CeHfZrSnErO_x$ architecture. Neither phase segregation of the $CeHfZrSnErO_x$ support nor Pd sintering was observed under thermal treatment up to 900°C. The as-afforded $Pd/CeHfZrSnErO_x$ catalyst exhibits good catalytic performance toward CO oxidation, outperforming Pd/CeO_2 of the same Pd loading, which highlights the inherent advantage of $CeHfZrSnErO_x$ as carrier support over traditional oxides.

INTRODUCTION

High-entropy oxides (HEOs) are among the emerging new classes of compositionally complex ceramics with abundant structural diversity and peculiar functional features which makes them promising candidates in various fields of applications including heterogeneous catalysis (Amiri and Shahbazian-Yassar, 2020; Rost et al., 2015; Sun and Dai, 2021; Zhang et al., 2021a, 2021b). As a unique class of concentrated solid-solution materials, HEOs, unlike high-entropy alloys (HEAs), possess independent cation and anion sublattices that give rise to expanded tuning range in composition and structure diversity (Chen et al., 2019; Sun and Dai, 2021). However, the potentials of HEOs as heterogeneous catalysts remain highly underexplored, partly due to the nascency of the high-entropy field but more importantly due to the unavailability of facile and reliable synthetic methods to fabricate nanostructured HEOs more suited for heterogeneous catalysis.

Since the emergence of the first HEO (rock-salt-structured) in 2015, there has been a growing interest in the development of synthetic strategies to fabricate HEO materials of other crystalline structures and functional features, including perovskite oxides (Okejiri et al., 2020), pyrochlores (Andrew et al., 2020), spinel oxides (Nguyen et al., 2020), fluorite-structured oxides (Xu et al., 2020), etc. Fluorite-structured HEOs, in particular, have shown great applicability as oxidation catalysts owing to their excellent redox properties and good oxygen storage capacity (Xu et al., 2020). The ability to generate and modulate the oxygen vacancy concentration in the crystal lattice is particularly useful in improving the catalytic performance for different oxidation reactions (Sun and Dai, 2021; Xu et al., 2020). Their great tunability and inherent surface complexity provide an excellent opportunity to access superior catalytic features "hidden" in the unexplored central regions of a multicomponent phase space of higher orders, constituting an obvious advantage over the traditional fluorite-structured binary oxides such as CeO_2, HfO_2, or ZrO_2. Unfortunately, the reported synthesis methods are tedious, rigorous, or energy-intensive, typically requiring extreme temperatures and/or pressures, long reaction times, resulting in microsized particles with reduced surface areas that are ill-suited for catalytic applications. For example, Chen et al. and Gild et al. fabricated

[1]Department of Chemistry, The University of Tennessee, Knoxville, TN 37996, USA

[2]Chemical Sciences Division, Oak Ridge National Laboratory, Oak Ridge, TN 37831, USA

[3]Center for Nanophase Materials Sciences, Oak Ridge National Laboratory, Oak Ridge, TN 37831, USA

[4]Lead contact

*Correspondence:
yangz3@ornl.gov (Z.Y.),
dais@ornl.gov (S.D.)

https://doi.org/10.1016/j.isci.2022.104214

fluorite-structured HEO materials via high-energy ball milling methods (Chen et al., 2018b; Gild et al., 2018). However, the requirements of extreme synthetic conditions, including the ultrahigh temperature (1500°C–1800°C) and extended reaction times (6–24 h), limit its application in heterogeneous catalysis. Nanocrystalline fluorite-structured HEOs have been realized via the nebulized spray pyrolysis method at 1150°C and 900 mbar pressure (Chellali et al., 2019). While the scalability of this synthetic strategy is quite promising, the requirement of a highly sophisticated piece of equipment constitutes both technological and economic constraints. More recently, our group synthesized fluorite-structured HEO support via a combination of mechanical ball milling and subsequent calcination at 900°C (Xu et al., 2020), which was used to improve the reducibility of lattice oxygen and stabilize Pd single atoms (SAs), leading to enhanced catalytic performance. Other promising strategies that have been reported include co-precipitation (Spiridigliozzi et al., 2021), co-precipitation and peptization (Anandkumar et al., 2019), and hydrothermal synthesis methods (Spiridigliozzi et al., 2020), being limited by rigorous synthetic processes, multiple reaction procedures, and energy-intensive unit operations, respectively. In addition, the as-afforded fluorite-structure HEOs are in dense phase and exhibit inferior mass transfer in catalysis. The development of technologically feasible, facile, and reliable synthetic strategies capable of generating high-quality fluorite-structure HEOs with high stability and nanoporous architecture is still highly desirable, particularly in high-temperature gas transformation procedures requiring robust noble metal SAs or small nanoparticles (NPs).

The present study demonstrates a facile ultrasound-mediated co-precipitation strategy deployed toward the fabrication of single-phase, fluorite-structured HEO nanocatalysts. Within 15 min of ultrasound exposure, nanocrystalline HEO ($CeHfZrSnErO_x$) was obtained sonochemically under ambient conditions and without the unfavorable heat-treatment process encountered in other synthetic strategies. The as-afforded $CeHfZrSnErO_x$ is characterized by ultrasmall crystallites with high surface area and high oxygen vacancy concentration, which provided an opportunity to stabilize palladium SAs or highly dispersed small NPs within the $CeHfZrSnErO_x$ architecture to form $Pd/CeHfZrSnErO_x$. The as-afforded nanocatalysts demonstrated ultrahigh stability and sintering resistance under thermal treatment conditions at up to 900°C. Using CO oxidation as a probe reaction, the inherent advantage of $CeHfZrSnErO_x$ over traditional oxides as carrier supports is highlighted by the superior catalytic performance of $Pd/CeHfZrSnErO_x$ over Pd/CeO_2 of the same Pd loading. This technologically feasible, facile, and scalable synthetic strategy holds great promise toward the synthesis of nanostructured HEO systems with functional features and promising applications to afford robust supported noble metal SA catalysts.

RESULTS

Synthesis of $CeHfZrSnErO_x$ and $Pd/CeHfZrSnErO_x$

Ultrasound can be used to drive high-energy chemical reactions via the physical process of acoustic cavitation that provides a unique high-energy environment at such magnitude and timescale that is unattainable with conventional energy sources. The acoustic cavitation phenomenon is described as the formation, growth, and implosive collapse of microbubbles in liquids under ultrasound irradiation, which could be leveraged for efficient production of high entropy materials under mild conditions (Suslick and Price, 1999; Zhang et al., 2021a, 2021b). Recently, we exploited this unique high-energy environment toward the synthesis of nanostructured HEAs (Liu et al., 2019; Okejiri et al., 2021), and high-entropy perovskite oxide nanocatalysts (Okejiri et al., 2020). The present study seeks to investigate the feasibility of fabricating fluorite-structured HEO nanocatalysts using an ultrasound-mediated co-precipitation strategy. First, the following selection guidelines as suggested by Rost et al. and modified by Djenadic et al. were considered for the choice of the metal compositions to favor the formation of a single-phase HEO system: (i) cations of similar ionic radii are preferred over cations with profound ionic size mismatch; (ii) the possible binary oxides should not exhibit uniform crystal structure; and (iii) there should exist, at least, one binary oxide pair that does not exhibit complete solubility in the oxide binary phase diagram (Djenadic et al., 2017; Rost et al., 2015). In the assessment of these, the following cations with comparable ionic were utilized as the metal precursor (Shannon, 1976): Ce^{3+}, Hf^{4+}, Zr^{4+}, Sn^{4+}, and Er^{3+}.

To sonochemically synthesize $CeHfZrSnErO_x$, an aqueous solution of the metal precursors was added to a precipitating agent and instantaneously exposed to ultrasound irradiation for 15 min. Following the separation and drying processes, $CeHfZrSnErO_x$ was obtained as a crystalline powder without calcination. The synthetic procedure is schematically shown in Figure 1A. $CeHfZrSnErO_x$-stabilized palladium nanoclusters ($Pd/CeHfZrSnErO_x$) were synthesized by adding an alcoholic solution of a palladium precursor to presynthesized $CeHfZrSnErO_x$ under ultrasound exposure for 10 min.
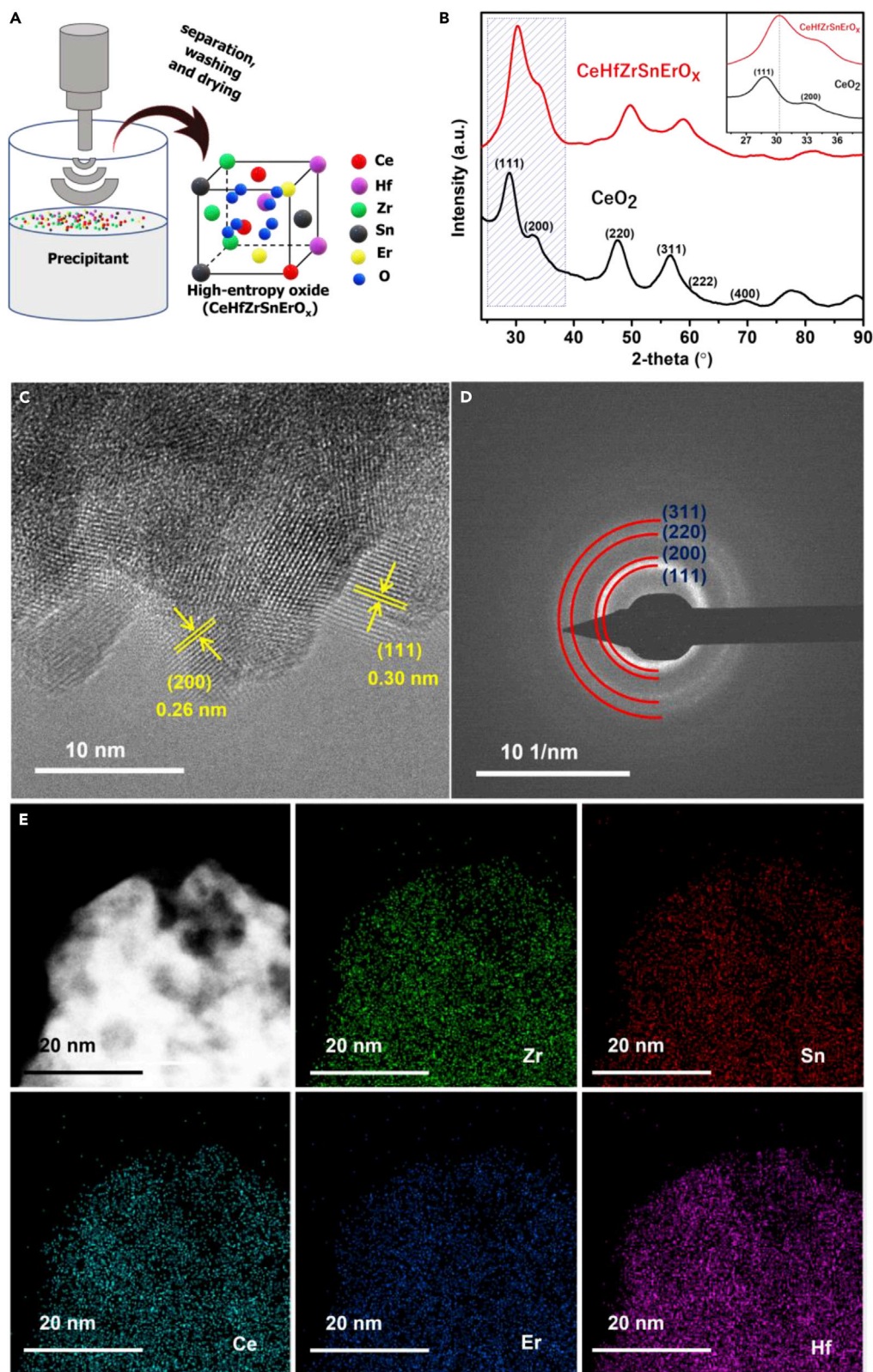
Figure 1. The synthesis and structure characterization of CeHfZrSnErOx

(A) Schematic illustration of the synthesis of CeHfZrSnErO$_x$.

Figure 1. *Continued*

(B) XRD patterns CeHfZrSnErO$_x$ and CeO$_2$ (the shift in reflection positions of CeHfZrSnErO$_x$ relative to CeO$_2$ is denoted by the dotted lines in the inset).

(C) HRTEM image of CeHfZrSnErO$_x$ and (D) the corresponding SAED.

(E) STEM-EDS elemental maps of CeHfZrSnErO$_x$ showing Zr (green), Sn (red), Ce (teal), Er (blue), and Hf (purple).

Structure characterization of CeHfZrSnErO$_x$

X-ray diffraction (XRD) technique was first employed for phase identification. Figure 1B displays the XRD patterns of CeHfZrSnErO$_x$ and CeO$_2$. The diffraction peaks of CeHfZrSnErO$_x$ are centered at 29.87°, 34.60°, 49.62°, 58.86°, 61.75°, and 72.57° and can be indexed to (111), (200), 220), (311), (222), and (400) planes, respectively, of a cubic fluorite structure. Compared to the diffraction pattern of CeO$_2$, these characteristic reflections are located at slightly higher 2-theta angles (inset in Figure 1B), suggesting a unique set of lattice parameters smaller than that of CeO$_2$. This shrinkage in the lattice parameter, from 5.4111 Å to 5.1911 Å, is consistent with the diffusion of the smaller-sized cations (Hf^{4+}, Zr^{4+}, Sn^{4+}, and Er^3) into the base CeO$_2$ crystal lattice to form CeHfZrSnErO$_x$ as a new single-phase HEO material. Notably, the peaks are sufficiently broad which generally suggest small crystallite size, microstrain, sample inhomogeneity, or instrumental effects (Zamkovskaya et al., 2018). But since the sample is compositionally homogeneous (as demonstrated later by the energy-dispersive X-ray (EDX) mapping), the crystallite size and microstrain contributions to peak broadening were assessed by the Williamson-Hall (W-H) method (Williamson and Hall, 1953) after correcting for the instrumental profile (Figure S1). Figure S2 displays the broadening in FWHM against 2-theta values obtained for the standard Si sample used for instrumental correction. A polynomial fitting of the experimentally observed values was made using the quadratic function in Equation 1:

$$y = ax^2 + bx + c \qquad \text{(Equation 1)}$$

where y is the broadening (FWHM), x is the 2-theta angle (°), a, b, and c are constants determined as 7.4 × $^{-6}$, −3.1 × 10^{-4}, and 0.13329, respectively (Figure S2). Figure S3 displays the plot of βcosθ against 4sinθ. The negative slope of the fitted line in the W-H plot indicates compressional strain and agrees with the contraction of the lattice parameter reported above. The estimated slope and hence the value of the microstrain is −0.0058, while the determined crystallite size is 6.3 nm. On the basis of these analyses, we conclude that the peak broadness is mainly due to the small crystallite size.

High-resolution transmission electron microscopy (HRTEM) images were acquired to gain additional structural information. Figure 1C displays the HRTEM image of the as-obtained CeHfZrSnErO$_x$ nanocrystals. The well-defined lattice fringes indicate high crystallinity. The interplanar spacings between lattice fringes were measured to be ∼0.30 and 0.26 nm, corresponding to the (111) and (200) planes of a cubic fluorite lattice. The corresponding selected area electron diffraction (SAED) pattern exhibits a continuous ring pattern, indicating its polycrystalline nature. The radial intensity line profile as a function of distance in the reciprocal lattice is shown in Figure 1D. The interplanar spacings agree with the values obtained from the XRD pattern and can be indexed to (111), (200), (220), and (311) planes of a cubic fluorite structure. Figure 1E displays the EDX elemental map of CeHfZrSnErO$_x$. The uniform distribution Ce, Hf, Zr, Sn, Er, and O in the nanosphere validate the formation of a single-phase HEO solid-solid. To demonstrate uniformity, the EDX elemental map of a different area of the sample was examined. The result (Figure S4) indicates that CeHfZrSnErO$_x$ is both chemically and structurally uniform.

The relative concentrations of the cations were determined by inductively coupled plasma optical emission spectroscopy (ICP-OES) analysis. The atomic percentages of Ce, Hf, Zr, Sn, and Er in the sample were determined to be 3.81, 3.73, 3.68, 3.72, and 3.71, respectively, which are consistent with the theoretical concentrations in the precursor solution. The slight deviation from equimolar stoichiometric ratios is probably due to the differences in the purity of the metal precursors.

The low-temperature N$_2$ adsorption isotherm and the corresponding pore size distribution of CeHfZrSnErO$_x$ are displayed in Figure S5. CeHfZrSnErO$_x$ exhibits a relatively high surface area (87 m^{2}g^{-1}) and a narrow pore size (5 nm) distribution which makes it a suitable candidate for the dispersion of active metal catalysts.

Surface chemistry analysis of CeHfZrSnErO$_x$

To understand the surface chemistry, X-ray photoelectron spectroscopy (XPS) technique was employed. Figure S6 displays the XPS survey spectrum of CeHfZrSnErO$_x$, showing photoemission signals for Ce, Hf,
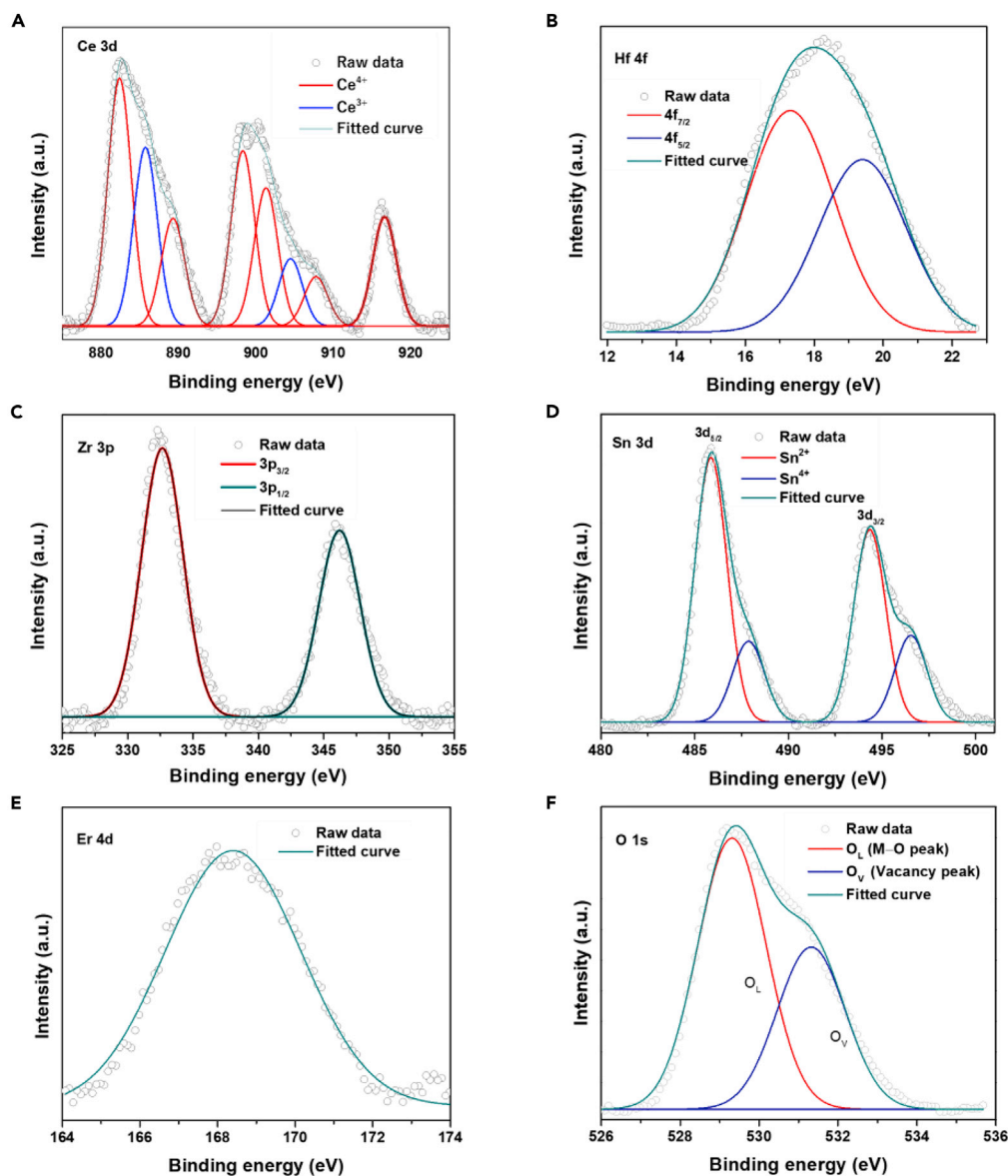
Figure 2. Core-level XPS spectra of CeHfZrSnErO$_x$

(A) Ce 3d.
(B) Hf 4f.
(C) Zr 3p.
(D) Sn 3d.
(E) Er 4d, and (F) O 1s.

Zr, Sn, Er, and O as expected. To gain insight into their oxidation states, the core-level spectra of Ce 3d, Hf 4f, Zr 3p, Sn 3d, Er 4d, and O 1s were acquired and displayed in Figures 2A–2F. For the Ce 3d XPS spectrum, eight peaks resulting from the pairs of spin-orbit doublets were identified through deconvolution. The six peaks centered at approximately 883, 888, 898, 901, 907, and 916 eV are assigned to Ce^{4+} species, while the two peaks around 885 and 905 eV are assigned to Ce^{3+} species (Han et al., 2016; He et al., 2019). The Hf 4f peak overlapped with a Ce 5p peak at ∼19 eV. Peak fitting reveals that the Hf 4f$_{7/2}$ is centered at 17.2 eV, and is normally attributed with Hf in the +4 oxidation state (Barreca et al., 2007). The Zr 3p spectrum contains two peaks with binding energies around 333 and 346 eV, characteristic of Zr^{+4} species (Huang et al., 2001; Yang et al., 2019). For the Sn 3d spectrum, four peaks were identified resulting from pairs of spin-orbit doublets. Two peaks centered at approximately 488 and 496 eV are assigned to Sn^{4+} species, while the

ones around 486 and 494 eV are attributed to Sn^{2+} species (Su et al., 2014; Xia et al., 2014). The Er photo-electron signal indicates that Erbium is unquestionably present in the sample's surface. However, the Er 4d peak overlapped with the Zr 3d signal. The peak fitting process is quite ambiguously given that the Er 4d photoelectron region consists of a complex mixture of doublets and satellite peaks not reliably identified at this point. Nevertheless, the approximate position of the Er 4d peak is consistent with the position of Er_2O_3 reported by Swami et al. (1984). The O 1s spectrum shows two peaks corresponding to two kinds of oxygen species. The strong peak at 529.5 eV is ascribed to the lattice oxygen (O_L), as in M—O (where M = Ce^{4+}, Ce^{3+} Hf^{4+}, Zr^{4+}, Sn^{4+}, and Er^{3+}); the other portion of the deconvoluted peak centered at 531 eV is attributed to oxygen vacancy O_V (Huang et al., 2014). Overall, the surface features of $CeHfZrSnErO_x$ are dominated by Ce^{4+}, Ce^{3+} Hf^{4+}, Zr^{4+}, Sn^{4+}, Sn^{2+}, Er^{3+}, and $O^{\delta-}$ species. The existence of Ce^{3+}, Sn^{2+}, and Er^{3+} suggests high surface oxygen vacancy concentration, which benefits reactant activation and conversion is catalytic CO oxidation (Gunawan et al., 2019).

Structure characterization of Pd/CeHfZrSnErO_x

After introducing 0.5–1.0 wt % Pd to $CeHfZrSnErO_x$, the diffraction pattern of the resultant $CeHfZrSnErO_x$-stabilized palladium nanoclusters ($Pd/CeHfZrSnErO_x$), like $CeHfZrSnErO_x$, displayed only diffraction peaks indexed to the cubic fluorite structure with no additional peak attributed to Pd or PdO species, indicating that Pd exists in the form of SAs or ultrasmall and highly dispersed NPs. However, the characteristic reflections progressively shifted (Figure 3A) toward the lower 2-theta angle with increasing Pd loading because of the substitution of a significant amount of Pd^{2+} for M^{n+} (M = Ce^{4+}, Hf^{4+}, Zr^{4+}, Sn^{4+}, or Er^{3+}) in $CeHfZrSnErO_x$ to form $PdCeHfZrSnErO_x$ as a new oxide phase with increased oxygen vacancy concentration and higher surface area relative to pristine $CeHfZrSnErO_x$ (Figure 3B). More importantly, Pd/$CeHfZrSnErO_x$ retained its single-phase cubic fluorite structure even after heat treatment at 500°C and 900°C (Figure S7). There were no apparent Pd peaks, highlighting the ability of $CeHfZrSnErO_x$ to stabilize metal species at elevated temperatures.

Scanning transmission electron microscopy (STEM) was used to observe the microstructure of Pd in Pd/$CeHfZrSnErO_x$. Unfortunately, owing to the lack of distinct contrast between Pd and the substrate, the highly dispersed/incorporated Pd species cannot be differentiated from the support. Notwithstanding, the EDS elemental map analysis displayed in Figure 3C reveals homogeneous distribution Pd, Ce, Hf, Zr, Sn, Er, and O with virtually no agglomeration of Pd species. The HRTEM image in Figure 3D shows well-defined lattice fringes with measured interplanar spacings of 0.30 and 0.26 nm, which correspond to the (111) and (200) planes, respectively, of the cubic fluorite structure. Additional lattice fringes with a measured d-spacing of 0.22 nm are equally visible and consistent with the (111) plane of the fcc lattice of Pd in accordance with the literature (Slavinskaya et al., 2016). Notably, these highly dispersed, low concentrated, ultrasmall-sized Pd nanocrystals were not detectable by XRD even after a slow scan of the Pd (111) region ($2\theta \approx 40$). Similarly, the SAED pattern in Figure 3E shows a diffuse ring that can be indexed to (111), (200), (220), and (311) planes of a cubic fluorite structure as well as an additional ring that is ascribed to the Pd (111) planes. This observation is in agreement with the HRTEM results. The relative concentrations of Pd in $Pd_{1.0}/CeHfZrSnErO_x$ (1.05%) and $Pd_{0.5}/CeHfZrSnErO_x$ (0.49%) were determined by ICP-OES and agree with the theoretical values.

Surface chemistry analysis of Pd/CeHfZrSnErO_x

Figure 4A displays the Pd 3d XPS spectrum of Pd/$CeHfZrSnErO_x$. The photoemission signals overlapped with the Zr 3p. Four peaks resulting from the pairs of spin-orbit doublets were identified for the Pd 3d XPS spectrum after deconvolution. Judging from the asymmetric peak shape and positions, it appears as though Pd exits as a combination of Pd^0 and Pd^{+2}. The peaks at 340 and 335 eV are attributed to $3d_{3/2}$ and $3d_{5/2}$ spin-orbits of metallic Pd^0 while those at 342 and 337 eV are ascribed to $3d_{3/2}$ and $3d_{5/2}$ spin-orbits of ionic Pd^{2+} in accordance with the literature (Gao et al., 2021; Mandapaka and Madras, 2016; Pillo et al., 1997; Priolkar et al., 2002; Ren et al., 2020). This submission is collaborated by the Pd CO adsorption behavior in the diffuse reflectance infrared Fourier transform spectroscopy (DRIFTS) spectra displayed in Figure 4B. The electron-deficient Pd^{2+} may have resulted from pairs of electron transfer from Pd to M through Pd-O-M bonds (M = Ce, Hf, Zr, Sn, and Er) in $PdCeHfZrSnErO_x$ solid solution as similarly reported elsewhere in the literature (Xu et al., 2020).

To further understand the chemical structure of palladium, additional information was acquired by the DRIFTS technique upon CO adsorption. The IR spectra are displayed in Figure 4B. To enhance the CO
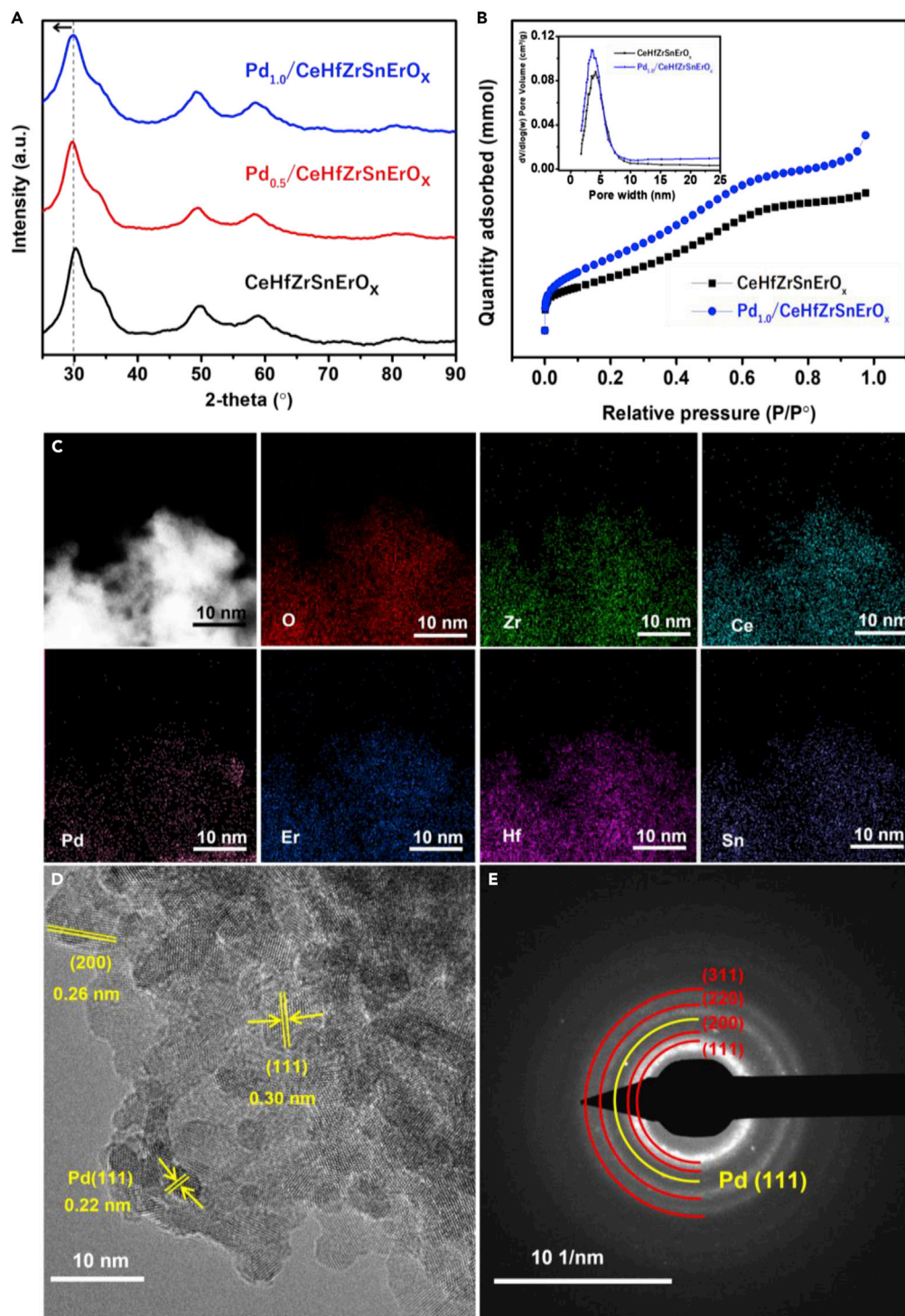
Figure 3. Structure characterization of CeHfZrSnErO$_x$ and Pd/CeHfZrSnErO$_x$

(A) XRD patterns of Pd/CeHfZrSnErO$_x$ and CeHfZrSnErO$_x$; the characteristic reflections progressively shifted toward the lower 2-theta angle with increasing Pd loading from 0.5–1.0 wt%.

(B) N$_2$ adsorption isotherms of CeHfZrSnErO$_x$ and Pd$_{1.0}$/CeHfZrSnErO$_x$ and the corresponding pore size distribution (inset).

(C) STEM-EDS elemental maps of CeHfZrSnErO$_x$ showing O (red), Zr (green), Ce (teal), Pd (pink), Er (blue), Hf (purple), and Sn (slate blue).

(D) HRTEM image of Pd$_{1.0}$/CeHfZrSnErO$_x$ and (E) the corresponding SAED.
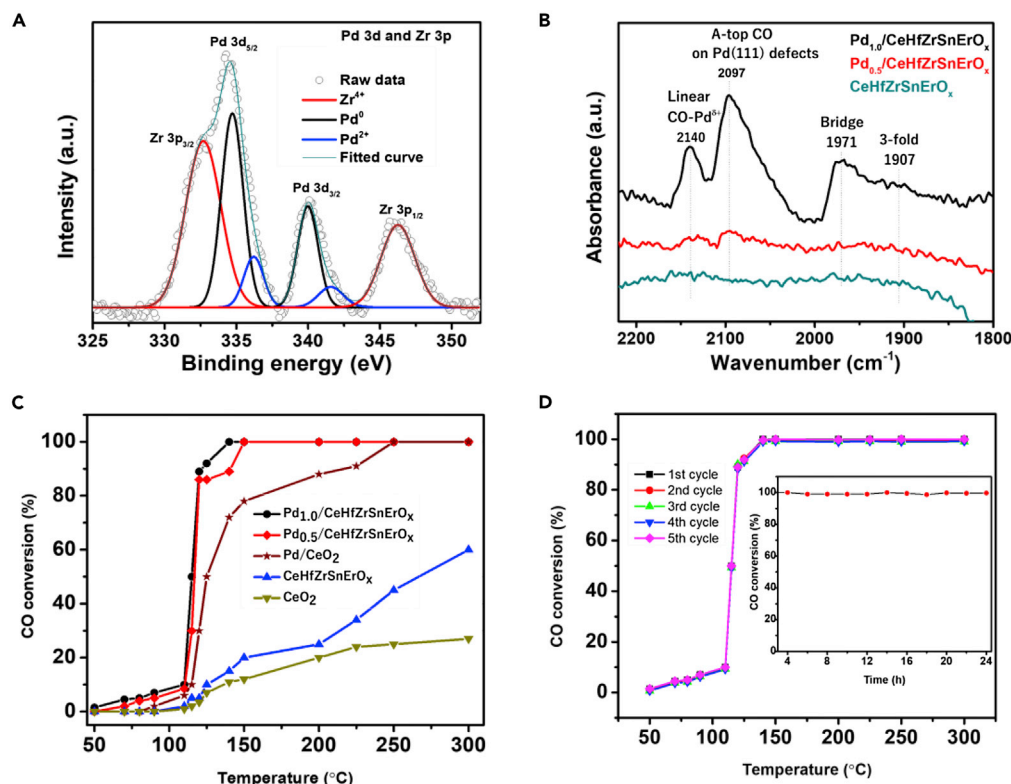
Figure 4. Surface chemistry characterization and catalytic performance evaluation
(A) Pd 3d XPS spectrum of $Pd_{1.0}/CeHfZrSnErO_x$.
(B) DRIFTS spectra of $Pd_{1.0}/CeHfZrSnErO_x$, $Pd_{0.5}/CeHfZrSnErO_x$, and $CeHfZrSnErO_x$ upon CO adsorption.
(C) Light-off curves of CO conversion over $Pd_{1.0}/CeHfZrSnErO_x$, $Pd_{0.5}/CeHfZrSnErO_x$, Pd/CeO_2, $CeHfZrSnErO_x$, and CeO_2. Reaction condition: 20 mg catalysts loading, 1% CO balanced with dry air at a flow rate of 12.5 mL/min.
(D) Cycled measurement of CO oxidation over $Pd_{1.0}/CeHfZrSnErO_x$ and its stability test result for a continuous CO oxidation experiment conducted at 140°C for 24 h (inset) and 100 h (Figure S9).

adsorption on the Pd sites, the samples were heated in the DRIFTS cell at 400°C for 30 min under 5% O_2/Ar flow to remove surface-bound organic residues that may have originated from ethylene glycol employed as the reducing agent-cum-solvent-cum-stabilizer in the synthesis process. The DRIFTS spectra of CO collected at 30°C show the existence of different active sites on the Pd-containing samples. For $Pd_{1.0}/CeHfZrSnErO_x$ with 1.0 wt% Pd, the IR bands at ~2097 cm^{-1} and ~2140 cm^{-1} are attributed to CO adsorbed onto A-top sites of Pd (111) atoms and linearly adsorbed CO on electron-deficient $Pd^{\delta+}$, respectively (Bertarione et al., 2006; Szanyi et al., 1993; Tiznado et al., 2004; Zaera, 2002). The less intense peak at ~1917 cm^{-1} is attributed to CO adsorbed on the bridge sites. The IR band signal for a 3-fold hollow site is virtually non-existent which indicates the absence of agglomerated Pd particles. The existence of both linear and bridge CO adsorption sites indicates the presence of single-sites and ensemble Pd sites, respectively (Zeinalipour-Yazdi et al., 2016). That said, it appears that that adsorption site is predominantly single-sites, judging from the relative intensities of both peaks. The IR spectrum of $Pd_{0.5}/CeHfZrSnErO_x$ with lower Pd loading displays only IR bands that are assignable to linearly bonded CO on Pd^{2+} and Pd^0 (111) defects, with no evidence of bridge nor hollow-CO bands, indicating that Pd is atomically dispersed on $CeHfZrSnErO_x$ carrier for this sample. On the other hand, the IR spectrum of $CeHfZrSnErO_x$ in the same wavenumber region, showed no characteristic IR band, suggesting its inability to adsorb CO molecules.

Catalytic CO oxidation, apparent activation energies, and stability tests

Catalytic CO oxidation is one of the most widely investigated reactions in heterogeneous catalysis because of its usefulness in both fundamental studies and pollution abatement (Chen et al., 2018a, 2020; Zhou et al., 2015). Catalytic CO oxidation, particularly over Pd-based has attracted significant interest in the research community because of its high performance and the relative simplicity of the process (Chen et al., 2018a,

2020; Zhou et al., 2015). Therefore, temperature-dependent CO oxidation was used as a model reaction to assess the activity of different catalytic materials synthesized in the present study. As seen in Figure 4C, the activity of the catalytic materials investigated in the present depends strongly on the Pd content and the support system and decreases in the following order: $Pd_{1.0}/CeHfZrSnErO_x \geq Pd_{0.5}/CeHfZrSnErO_x \gg Pd_{1.0}/CeO_2 \gg CeHfZrSnErO_x > CeO_2$. Their apparent activation energies were calculated and displayed in Figure S8. The order of the determined apparent activation energies is consistent with the order of the activity of the five catalysts and is given as follow: CeO_2 (118.5 kJ/mol) > $CeHfZrSnErO_x$ (96.2 kJ/mol) $\gg$ Pd_1/CeO_2 (75.8 kJ/mol) $\geq Pd_{0.5}/CeHfZrSnErO_x$ (29.5 kJ/mol) $\geq Pd_{1.0}/CeHfZrSnErO_x$ (23.8 kJ/mol). Among the various $CeHfZrSnErO_x$-based catalysts investigated, pristine $CeHfZrSnErO_x$ exhibited the least activity for CO oxidation with a high onset temperature of 110°C with no complete CO conversion below 300°C as seen in Figure 4C. The introduction of 0.5 or 1.0 wt% Pd to pristine $CeHfZrSnErO_x$ dramatically improved its catalytic performance. The resultant $Pd_{0.5}/CeHfZrSnErO_x$ and $Pd_{1.0}/CeHfZrSnErO_x$ showed lower onset temperatures of $\sim$50°C and 70°C, respectively, and a complete CO oxidation at 140°C and 150°C, respectively, indicating the significant importance of the highly dispersed Pd species within the HEO system. The presence of Pd facilitates the CO and O_2 adsorption on the catalysts' surface, which in turn resulted in higher catalytic activity (Kunkalekar and Salker, 2012).

Interestingly, the ceria-supported Pd catalyst Pd/CeO_2 exhibited inferior performance relative to $Pd_{0.5}/CeHfZrSnErO_x$ and $Pd_{1.0}/CeHfZrSnErO_x$ but superior to pristine $CeHfZrSnErO_x$ under similar conditions. The onset and complete conversion temperatures, over Pd/CeO_2, are 90°C and 250°C, respectively. It should be noted that CO oxidation over reducible oxide-supported metal catalysts is generally believed to proceed via the Mars-Van-Krevelen reaction mechanism, where the adsorbed CO on the metals interacts with active lattice O from the reducible support to create oxygen vacancies (Peterson et al., 2014); hence, the reducibility of the surface lattice O from the support significantly impacts the catalytic CO oxidation (Xu et al., 2020). Therefore, it is reasonable to posit that superior catalytic performance of $Pd_{0.5}/CeHfZrSnErO_x$ and $Pd_{1.0}/CeHfZrSnErO_x$ over Pd/CeO_2 is most likely due to enhanced reducibility of the surface lattice oxygen in the vicinity of the Pd in addition to the high oxygen vacancy concentration in the crystal lattice. This is consistent with the experimental result previously reported (Xu et al., 2020). Also, a strong synergistic effect that goes beyond the simple additive result of combining five catalytically active metals in the cation sublattice may have also contributed to the superior activity. Similarly, the catalytic performance of pristine $CeHfZrSnErO_x$ is superior to that of pure ceria under identical test conditions, additionally highlighting the inherent advantage of $CeHfZrSnErO_x$ as the carrier support.

Furthermore, the stability test of $Pd_{1.0}/CeHfZrSnErO_x$ was studied via a continuous CO oxidation experiment conducted at 140°C for 24 h. $Pd_{1.0}/CeHfZrSnErO_x$ showed remarkable stability for CO oxidation, displaying no appreciable loss of activity for 24 and 100 h as seen in Figures 4D (inset) and S9. Additionally, the reusability was tested through consecutive CO oxidation experiments for five cycles. As seen in Figure 4D, $Pd_{1.0}/CeHfZrSnErO_x$ maintains its low-temperature CO oxidation and good reproducibility of results across all five use cycles.

DISCUSSION

In summary, we have developed an ultrasound-mediated co-precipitation strategy to fabricate nanostructured high-entropy fluorite oxide ($CeHfZrSnErO_x$) without any external heat treatment. The chemical effect and crystallization process are driven by the transient localized hotspot generated by the physical phenomenon of acoustic cavitation. The as-synthesized $CeHfZrSnErO_x$ carrier, given its high surface area and high oxygen vacancy concentration, was employed as an excellent carrier for the stabilization of highly dispersed palladium species. The $CeHfZrSnErO_x$-stabilized Pd catalysts ($Pd/CeHfZrSnErO_x$) outperformed a ceria-stabilized counterpart (Pd/CeO_2) toward catalytic CO oxidation, underscoring the inherent advantage of $CeHfZrSnErO_x$ as reducible carrier support. Such a technologically feasible, scalable, and facile synthetic strategy holds great promise toward the synthesis of HEO systems of other crystal structures and functionalities and the development of robust SAs-derived nanocatalysts.

Limitations of the study

A facile synthesis of fluorite-structured high-entropy oxide nanocatalysts is described in the present study. However, it would be pertinent to investigate the synthetic protocol toward the fabrication of high-entropy oxide systems of different crystal structures and functional features, namely perovskite oxides, pyrochlores, spinel oxides, etc., before generalizing the synthetic method.

STAR★METHODS

Detailed methods are provided in the online version of this paper and include the following:

- KEY RESOURCES TABLE
- RESOURCE AVAILABILITY
  - ○ Lead contact
  - ○ Materials availability
  - ○ Data and code availability
- METHOD DETAILS
  - ○ Synthesis of CeHfZrSnErO$_x$
  - ○ Synthesis of Pd/CeHfZrSnErO$_x$
  - ○ Sythesis of CeO$_2$
  - ○ Synthesis of Pd/CeO$_2$
  - ○ Characterization techniques
  - ○ Catalytic CO oxidation experiment
- QUANTIFICATION AND STATISTICAL ANALYSIS

AUTHOR CONTRIBUTIONS

F.O., Z.Y., and S.D. conceived the research idea. F.O. performed the experiments and carried out some of the measurements. Z.H and M.C. performed the microscopy measurements; F.G. performed the CO DRIFTS measurement. Z.Y. and S.D. provided valuable improvements for the overall experiments. J.F. and F.O. analyzed the XPS data. F.O., Z.Y., and S.D. co-wrote and revised the paper. All authors discussed the results, raised suggestions, and commented on the manuscript.

DECLARATION OF INTERESTS

The authors declare no competing interests.

REFERENCES

Amiri, A., and Shahbazian-Yassar, R. (2020). Recent progress of high-entropy materials for energy storage and conversion. J. Mater. Chem. A 9, 782–823.

Anandkumar, M., Bhattacharya, S., and Deshpande, A.S. (2019). Low temperature synthesis and characterization of single phase multi-component fluorite oxide nanoparticle sols. RSC Adv. 9, 26825–26830.

Andrew, J.W., Wang, Q., Hu, C., Yeh, Y.-T., Chen, R., and Luo, J. (2020). Single-phase duodenary high-entropy fluorite/pyrochlore oxides with an order-disorder transition. Preprint at arXiv. https://doi.org/10.1016/j.actamat.2021.116858.

Barreca, D., Milanov, A., Fischer, R., Devi, A., and Tondello, E. (2007). Hafnium oxide thin film grown by ALD: an XPS study. Surf. Sci. Spectra. 14, 34–40.

Bertarione, S., Prestipino, C., Groppo, E., Scarano, D., Spoto, G., Zecchina, A., Pellegrini, R., Leofanti, G., and Lamberti, C. (2006). Direct IR observation of vibrational properties of carbonyl species formed on Pd nano-particles supported on amorphous carbon: comparison with Pd/SiO2–Al2O3. Phys. Chem. Chem. Phys. 8, 3676–3681.

Chellali, M.R., Sarkar, A., Nandam, S.H., Bhattacharya, S.S., Breitung, B., Hahn, H., and Velasco, L. (2019). On the homogeneity of high entropy oxides: an investigation at the atomic scale. Scripta Mater. 166, 58–63.

Chen, H., Fu, J., Zhang, P., Peng, H., Abney, C.W., Jie, K., Liu, X., Chi, M., and Dai, S. (2018a). Entropy-stabilized metal oxide solid solutions as CO oxidation catalysts with high-temperature stability. J. Mater. Chem. A 6, 11129–11133.

Chen, H., Jie, K., Jafta, C.J., Yang, Z., Yao, S., Liu, M., Zhang, Z., Liu, J., Chi, M., Fu, J., and Dai, S. (2020). An ultrastable heterostructured oxide catalyst based on high-entropy materials: a new strategy toward catalyst stabilization via synergistic interfacial interaction. Appl. Catal. B Environ. 276, 119155.

Chen, K., Pei, X., Tang, L., Cheng, H., Li, Z., Li, C., Zhang, X., and An, L. (2018b). A five-component entropy-stabilized fluorite oxide. J. Eur. Ceram. Soc. 38, 4161–4164.

Chen, P.-C., Liu, M., Du Jingshan, S., Meckes, B., Wang, S., Lin, H., Dravid Vinayak, P., Wolverton, C., and Mirkin Chad, A. (2019). Interface and heterostructure design in polyelemental nanoparticles. Science 363, 959–964.

Djenadic, R., Sarkar, A., Clemens, O., Loho, C., Botros, M., Chakravadhanula, V.S.K., Kübel, C., Bhattacharya, S.S., Gandhi, A.S., and Hahn, H. (2017). Multicomponent equiatomic rare earth oxides. Mater. Res. Lett. 5, 102–109.

Gao, J., Ren, C., Huo, X., Ji, R., Wen, X., Guo, J., and Liu, J. (2021). Supported palladium catalysts: a facile preparation method and implications to reductive catalysis technology for water treatment. ACS ES&T Eng. 1, 562–570.

Gild, J., Samiee, M., Braun, J.L., Harrington, T., Vega, H., Hopkins, P.E., Vecchio, K., and Luo, J. (2018). High-entropy fluorite oxides. J. Eur. Ceram. Soc. 38, 3578–3584.

Gunawan, C., Lord, M.S., Lovell, E., Wong, R.J., Jung, M.S., Oscar, D., Mann, R., and Amal, R. (2019). Oxygen-vacancy engineering of cerium-oxide nanoparticles for antioxidant activity. ACS Omega 4, 9473–9479.

Han, J., Meeprasert, J., Maitarad, P., Nammuangruk, S., Shi, L., and Zhang, D. (2016). Investigation of the facet-dependent catalytic performance of Fe2O3/CeO2 for the selective catalytic reduction of NO with NH3. J. Phys. Chem. C 120, 1523–1533.

He, L., Ren, Y., Fu, Y., Yue, B., Tsang, S., and He, H. (2019). Morphology-dependent catalytic activity of Ru/CeO2 in dry reforming of methane. Molecules 24, 526.

Huang, C., Tang, Z., and Zhang, Z. (2001). Differences between zirconium hydroxide (Zr(OH)4·nH2O) and hydrous zirconia (ZrO2·nH2O). J. Am. Ceram. Soc. 84, 1637–1638.

Huang, H., Dai, Q., and Wang, X. (2014). Morphology effect of Ru/CeO2 catalysts for the catalytic combustion of chlorobenzene. Appl. Catal. B Environ. 158–159, 96–105.

Kunkalekar, R.K., and Salker, A.V. (2012). Activity of Pd doped and supported Mn2O3 nanomaterials for CO oxidation. React. Kinet. Mech. Catal. 106, 395–405.

Liu, M., Zhang, Z., Okejiri, F., Yang, S., Zhou, S., and Dai, S. (2019). Entropy-maximized synthesis of multimetallic nanoparticle catalysts via a ultrasonication-assisted wet chemistry method under ambient conditions. Adv. Mater. Inter. 6, 1900015.

Mandapaka, R.K., and Madras, G. (2016). Microkinetic modeling of CO oxidation on ionic palladium-substituted ceria. Ind. Eng. Chem. Res. 55, 2309–2318.

Nguyen, T.X., Patra, J., Chang, J.-K., and Ting, J.-M. (2020). High entropy spinel oxide nanoparticles for superior lithiation–delithiation performance. J. Mater. Chem. A 8, 18963–18973.

Okejiri, F., Yang, Z., Chen, H., Do-Thanh, C.-L., Wang, T., Yang, S., and Dai, S. (2021). Ultrasound-driven fabrication of high-entropy alloy nanocatalysts promoted by alcoholic ionic liquids. Nano Res. 14, 1–7.

Okejiri, F., Zhang, Z., Liu, J., Liu, M., Yang, S., and Dai, S. (2020). Room-temperature synthesis of high-entropy perovskite oxide nanoparticle catalysts through ultrasonication-based method. ChemSusChem 13, 111–115.

Peterson, E.J., Delariva, A.T., Lin, S., Johnson, R.S., Guo, H., Miller, J.T., Hun Kwak, J., Peden, C.H.F., Kiefer, B., Allard, L.F., et al. (2014). Low-temperature carbon monoxide oxidation catalysed by regenerable atomically dispersed palladium on alumina. Nat. Commun. 5, 4885.

Pillo, T., Zimmermann, R., Steiner, P., and Hüfner, S. (1997). The electronic structure of PdO found by photoemission (UPS and XPS) and inverse photoemission (BIS). J. Phys. Condens. Matter 9, 3987–3999.

Priolkar, K.R., Bera, P., Sarode, P.R., Hegde, M.S., Emura, S., Kumashiro, R., and Lalla, N.P. (2002). formation of Ce1-xPdxO2-δ solid solution in combustion-synthesized Pd/CeO2 catalyst: XRD, XPS, and EXAFS investigation. Chem. Mater. 14, 2120–2128.

Ren, C., Yang, P., Gao, J., Huo, X., Min, X., Bi, E.Y., Liu, Y., Wang, Y., Zhu, M., and Liu, J. (2020). Catalytic reduction of aqueous chlorate with MoOx immobilized on Pd/C. ACS Catal. 10, 8201–8211.

Rost, C.M., Sachet, E., Borman, T., Moballegh, A., Dickey, E.C., Hou, D., Jones, J.L., Curtarolo, S., and Maria, J.-P. (2015). Entropy-stabilized oxides. Nat. Commun. 6, 8485.

Shannon, R. (1976). Revised effective ionic radii and systematic study of inter atomic distances in halides and chalcogenides. Acta Crystallogr. A 32, 751–767.

Slavinskaya, E.M., Kardash, T.Y., Stonkus, O.A., Gulyaev, R.V., Lapin, I.N., Svetlichnyi, V.A., and Boronin, A.I. (2016). Metal–support interaction in Pd/CeO2 model catalysts for CO oxidation: from pulsed laser-ablated nanoparticles to highly active state of the catalyst. Catal. Sci. Technol. 6, 6650–6666.

Spiridigliozzi, L., Ferone, C., Cioffi, R., Accardo, G., Frattini, D., and Dell'Agli, G. (2020). Entropy-stabilized oxides owning fluorite structure obtained by hydrothermal treatment. Materials 13, 558.

Spiridigliozzi, L., Ferone, C., Cioffi, R., and Dell'Agli, G. (2021). A simple and effective predictor to design novel fluorite-structured High Entropy Oxides (HEOs). Acta Mater. 202, 181–189.

Su, S.C., Zhang, H.Y., Zhao, L.Z., He, M., and Ling, C.C. (2014). Band alignment of n-SnO2/p-GaN hetero-junction studied by x-ray photoelectron spectroscopy. J. Phys. D Appl. Phys. 47, 215102.

Sun, Y., and Dai, S. (2021). High-entropy materials for catalysis: a new Frontier. Sci. Adv. 7, eabg1600.

Suslick, K.S., and Price, G.J. (1999). Applications OF ultrasound to materials chemistry. Annu. Rev. Mater. Sci. 29, 295–326.

Swami, G.T.K., Stageberg, F.E., and Goldman, A.M. (1984). XPS characterization of erbium sesquioxide and erbium hydroxide. J. Vac. Sci. Technol. A 2, 767–770.

Szanyi, J., Kuhn, W., and Goodman, D. (1993). CO adsorption on Pd(111) and Pd(100): low and high pressure correlations. J. Vac. Sci. Technol. A Vac. Surf. Films 11, 1969–1974.

Tiznado, H., Fuentes, S., and Zaera, F. (2004). Infrared study of CO adsorbed on Pd/Al2O3−ZrO2. Effect of zirconia added by impregnation. Langmuir 20, 10490–10497.

Williamson, G.K., and Hall, W.H. (1953). X-ray line broadening from filed aluminium and wolfram. Acta Metall. 1, 22–31.

Xia, W., Wang, H., Zeng, X., Han, J., Zhu, J., Zhou, M., and Wu, S. (2014). High-efficiency photocatalytic activity of type II SnO/Sn3O4 heterostructures via interfacial charge transfer. CrystEngComm 16, 6841–6847.

Xu, H., Zhang, Z., Liu, J., Do-Thanh, C.-L., Chen, H., Xu, S., Lin, Q., Jiao, Y., Wang, J., Wang, Y., et al. (2020). Entropy-stabilized single-atom Pd catalysts via high-entropy fluorite oxide supports. Nat. Commun. 11, 1–9.

Yang, H., Zhang, J., Li, J., Shen, Q., and Zhang, L. (2019). In situ preparation and corrosion resistance of a ZrO2 film on a ZrB2 ceramic. Coatings 9, 455.

Zaera, F. (2002). Infrared and molecular beam studies of chemical reactions on solid surfaces. Int. Rev. Phys. Chem. 21, 433–471.

Zamkovskaya, A., Maksimova, E., and Nauhatsky, I. (2018). Size–strain line-broadening analysis of the calcite-type borates ABO3 (A=Fe, In, Ga). J. Phys. Conf. Ser. 1135, 012020.

Zeinalipour-Yazdi, C.D., Willock, D.J., Thomas, L., Wilson, K., and Lee, A.F. (2016). CO adsorption over Pd nanoparticles: a general framework for IR simulations on nanoparticles. Surf. Sci. 646, 210–220.

Zhang, S., Saji, S.E., Yin, Z., Zhang, H., Du, Y., and Yan, C.H. (2021a). Rare-Earth incorporated alloy catalysts: synthesis, properties, and applications. Adv. Mater. 33, 2005988.

Zhang, S., Zeng, Z., Li, Q., Huang, B., Zhang, X., Du, Y., and Yan, C.-H. (2021b). Lanthanide electronic perturbation in Pt–Ln (La, Ce, Pr and Nd) alloys for enhanced methanol oxidation reaction activity. Energ. Environ. Sci. 14, 5911–5918.

Zhang, Z., Yang, S., Hu, X., Xu, H., Peng, H., Liu, M., Thapaliya, B.P., Jie, K., Zhao, J., Liu, J., et al. (2019). Mechanochemical nonhydrolytic sol–gel strategy for the production of mesoporous multimetallic oxides. Chem. Mater. 31, 5529–5536.

Zhou, Y., Wang, Z., and Liu, C. (2015). Perspective on CO oxidation over Pd-based catalysts. Catal. Sci. Technol. 5, 69–81.

STAR★METHODS

KEY RESOURCES TABLE

REAGENT or RESOURCE	SOURCE	IDENTIFIER
Other		
Cerium (III) chloride heptahydrate (CeCl$_3$·H$_2$O)	Fischer chemicals, USA	CAS: 18618-55-8
Hafnium (IV) chloride (HfCl$_4$)	Alfa Aesar, USA	CAS: 13499-05-3
Zirconium (IV) chloride (ZrCl$_4$)	Sigma Aldrich, USA	CAS: 10026-11-6
Tin (IV) chloride hydrate (SnCl$_4$·xH$_2$O)	Alfa Aesar, USA	CAS: 7646-78-8
Erbium (III) nitrate pentahydrate	Alfa Aesar, USA	CAS: 10031-51-3
Sodium hydroxide	Sigma Aldrich, USA	CAS: 1310-73-2
Potassium tetrachloropalladate (II) (K$_2$PdCl$_4$)	Fischer chemicals, USA	CAS: 10025-98-6
Ethylene glycol (HO-CH$_2$CH$_2$-OH)	Alfa Aesar, USA	CAS: 107-21-1
Software and algorithms		
MDI JADE	Materials Data JADE	https://materialsdata.com/prodjd.html
OriginPro 2017	OriginLab	https://www.originlab.com/index.aspx?go=Products/Origin/2021b&pid=4416
Microsoft Excel	Microsoft	https://www.microsoft.com/en-gb/
Other		
PANalytical Empyrean diffractometer	Malvern Panalytical Ltd.	https://www.malvernpanalytical.com/en/products/product-range/empyrean-range/empyrean
Gemini 2375 surface area analyzer	Micromeritics Instrument Co.	https://www.micromeritics.com/particle-testing/analytical-testing/surface-area/
Hitachi HT-7700 microscope	Hitachi High-Tech in America	https://www.hitachi-hightech.com/us/library/literature/brochure-highresolution-lens-exalens-ht7700-transmission-electron-microscope.html
Thermo Nicolet Nexus 670 FTIR	ThermoFisher Scientific	https://www.thermofisher.com
DiffusIR	Pike Technologies	https://www.piketech.com/product/dr-diffusir-tm/
Thermo Scientific Model K-Alpha S5	ThermoFisher Scientific	https://www.thermofisher.com/us/en/home/electron-microscopy/products/xps-instruments/k-alpha.html
Agilent 5110 ICP-OES spectrometer	Agilent Technologies, Inc.	https://www.agilent.com/en/product/atomic-spectroscopy/inductively-coupled-plasma-optical-emission-spectroscopy-icp-oes/icp-oes-instruments/5110-icp-oes
750 Watt ultrasonic processor, VCX 750	Sonics & Materials, INC	https://www.sonics.com/?gclid=Cj0KCQjwt-6LBhDlARIsAIPRQcLOWvO1WqUzQzFUlJG7ecXoSyKEqXnNeTLgjmbKJQ1yzXpLnSv-mTIaAlG7EALw_wcB

RESOURCE AVAILABILITY

Lead contact

Further information and requests for resources and reagents should be directed to and will be fulfilled by the lead contact, Sheng Dai (dais@ornl.gov).

Materials availability

All materials generated in this study are available from the lead contact without restriction.

Data and code availability

All data reported in this paper will be shared by the lead contact upon request. This paper does not report original code. Any additional information required to reanalyze the data reported in this paper is available from the lead contact upon request.

METHOD DETAILS

Synthesis of CeHfZrSnErO$_x$

To synthesize CeHfZrSnErO$_x$, an aqueous solution of the metal precursors was prepared by dissolution of 1.0 mmol each of CeCl$_3$·7H$_2$O, HfCl$_4$, ZrCl$_4$, SnCl$_4$·xH$_2$O, and Er(NO$_3$)$_3$·5H$_2$O in 3.0 mL deionized (DI) water. The precursors were added dropwise to a 30.0 mL of 5.0 M NaOH solution while simultaneously being exposed to ultrasound irradiation for 15 min via direct immersion of an ultrasonic titanic horn operating at 20 kHz at ambient conditions, as schematically shown in Figure 1A. The ultrasonic processor which has a maximum output of 750 W was acquired from Sonics & Materials, INC. and equipped with a cylindrical probe of $^3/_4$″ diameter. The sonication was performed under the pulsed mode, and the amplitude was set at 50% amplitude. When the sonication time was reached, the solid was recovered via centrifugation, washed thoroughly with deionized (DI) water before being dried in an oven at 110°C to obtain the final crystallites.

For the investigation of the entropic contribution to phase stability, the as-synthesized CeHfZrSnErO$_x$ was heated at different temperatures and rapidly air-quenched to preserve the crystal structure at the specific temperature.

Synthesis of Pd/CeHfZrSnErO$_x$

To synthesize Pd/CeHfZrSnErO$_x$, an alcoholic solution the Pd precursor was prepared by dissolution 0.025 mmol of K$_2$PdCl$_4$ in 5.0 mL ethylene glycol. This solution was combined with a calculated mass of the as-synthesized CeHfZrSnErO$_x$ pre-dispersed in 30.0 mL ethylene glycol for a final Pd mass loading of 0.5 or 1.0 wt% (referred to as Pd$_{0.5}$/CeHfZrSnErO$_x$ and Pd$_{1.0}$/CeHfZrSnErO$_x$, respectively). This mixture was quickly exposed to ultrasound irradiation for 10 min via direct immersion of ultrasonic titanic horn operating at 20 kHz at ambient conditions. When the sonication time was reached, the solid was recovered via centrifugation, washed thoroughly with DI water and ethanol before being dried in an oven at 90°C to obtain CeHfZrSnErO$_x$-stabilized palladium nanoclusters (Pd/CeHfZrSnErO$_x$) as the final crystallite. Pd$_{1.0}$/CeHfZrSnErO$_x$ was chosen as the representative sample for characterization purposes except otherwise indicated. Also, Pd/CeO$_2$ with 1.0 wt% Pd was synthesized in a similar manner. The detailed synthetic procedure is provided in the supplementary information.

Sythesis of CeO$_2$

To synthesize CeO$_2$, an aqueous solution of the metal precursors was prepared by dissolution of 5.0 mmol of CeCl$_3$·7H$_2$O in 3.0 mL deionized (DI) water. The precursors were added dropwise to a solution of NaOH while simultaneously being exposed to ultrasound irradiation for 15 min via direct immersion of an ultrasonic titanic horn operating at 20 kHz at ambient conditions. When the sonication time was reached, the solid was recovered via centrifugation, washed thoroughly with DI water before being dried in an oven at 110°C to obtain the final crystallites.

Synthesis of Pd/CeO$_2$

To synthesize Pd/CeO$_2$, an alcoholic solution the Pd precursor was prepared by dissolution 0.025 mmol of K$_2$PdCl$_4$ in 5.0 mL ethylene glycol. This solution was combined with a calculated mass of the as-synthesized CeO$_2$ support pre-dispersed in 30.0 mL ethylene glycol for a final Pd mass loading of 1.0 wt%. This mixture was quickly exposed to ultrasound irradiation for 10 min via direct immersion of ultrasonic titanic horn operating at 20 kHz at ambient conditions. When the sonication time was reached, the solid was recovered via centrifugation, washed thoroughly with DI water and ethanol before being dried in an oven at 90°C to obtain Pd/CeO$_2$ as the final crystallite.

Characterization techniques

To determine the crystallographic structure of the materials, the X-ray diffraction (XRD) technique was employed. XRD patterns were acquired on a PANalytical Empyrean diffractometer with Cu Kα1 radiation (λ = 1.5406 Å), operated at 45 kV and 40 mA. The 2θ range angles were scanned between 20° to 90° at a step size of 0.05°. The crystallite size and microstrain contributions to peak broadening were assessed by Williamson–Hall (W–H) analysis (Williamson and Hall, 1953). The instrumental broadening effect was taken into account in the measurement of the full width at half maximum intensity (FWHM). A silicon standard sample was used to apply a correction for the instrumental broadening. The W-H analysis assumes

that the crystallite size and microstrain contributions are mutually independent of each other and is given by Equation 2:

$$\beta \cos \theta = \frac{K\lambda}{D} + 4\,\varepsilon \sin \theta \qquad \text{(Equation 2)}$$

where β is the FWHM in radians, θ is the scattered angle measured in degrees, k is the shape factor (0.9), λ is the wavelength of the X-ray (0.15406 nm), D and ε represent the crystallite size and microstrain, respectively. By plotting a graph of $\beta\cos\theta$ against $4\sin\theta$, the microstrain and average crystallite size were estimated by the slope of the line and y-intercept extrapolation, respectively. The interplanar spacings were determined by Bragg's law using MDI JADE 6.5 software. The lattice parameter, a_0 was calculated from Equation 3 after indexing the hkl values for each of the diffraction peaks.

$$d_{hkl} = \frac{a_o}{\sqrt{\left(h^2 + k^2 + l^2\right)}} \qquad \text{(Equation 3)}$$

The specific surface area of samples was determined by low-temperature (77 K) nitrogen adsorption performed on Gemini 2375 surface area analyzer. Prior to analysis, samples were degassed for 6 h in a drying compartment under N_2 at 160°C to eliminate any adsorbed species. Surface area analysis was performed by applying the Brunauer, Emmett, and Teller (BET) theory. Pore size distributions were calculated from the adsorption isotherm using Barrett–Joyner–Halenda (BJH) method. High-resolution transmission electron microscopy (HRTEM) images and the energy-dispersive X-ray spectroscopy (EDS) mapping images were recorded on Hitachi H-7700 microscope with an acceleration voltage of 100 kV. Diffuse reflectance infrared Fourier transform spectroscopy (DRIFTS) spectra were acquired on Thermo Nicolet Nexus 670 FTIR spectrometer equipped with a mercury cadmium telluride (MCT) detector and Pike Technologies diffuse reflectance cell. Each spectrum was recorded with 32 scans at a resolution of 4 cm^{-1}. In a typical run, the sample was loaded into a ceramic cup located in the DRIFTS cell and preheated at 400°C for 30 min under a constant flow of 5% O_2/Ar gas (flow rate $\approx$ 30 mL/min). Next, Ar was passed through the sample and the temperature was taken down to 30°C for background collection. Thereafter, CO was adsorbed for 10 min at 30°C, followed by desorption for 10 min at 30°C. Spectra were collected during the adsorption-desorption process and transformed into Kubelka-Munk form. X-ray photoelectron spectroscopy (XPS) spectra were recorded on Thermo Scientific Model K-Alpha S5 X-ray Photoelectron Spectrometer (XPS) System using Al Kα (1486.6 eV photons) as the radiation source. The instrument uses a hemispherical electron energy analyzer equipped with a 128-channel electron detection system. Samples were prepared for analysis by dispersing the powder material onto a double-sided tape fixed to a clean glass slide. After inserting the sample into the analysis chamber through a vacuum-pumped load-lock, an initial wide energy range survey scan was acquired. Next, a set of narrow energy range core level spectra were acquired for the elements of interest. The C 1s peak (284.6 eV) was used for the calibration. The relative metal concentrations were determined by inductively coupled plasma optical emission spectroscopy (ICP-OES) analysis performed on an Agilent 5110 ICP-OES spectrometer. Prior to analysis, samples were digested in aqua regia and diluted with 2.0% nitric acid.

Catalytic CO oxidation experiment

The catalytic CO oxidation experiment was performed in a fixed-bed reactor at atmospheric pressure conditions according to previous reports (Okejiri et al., 2020; Zhang et al., 2019). The reactor is made of quartz tubing with an inner diameter of approximately 4 mm. The gas flow rate was controlled with a mass-flow controller. For the measurement of CO light-off curves showing CO conversion as a function of reaction temperature, 20 mg of the catalyst was charged into the reactor and supported with a ball of quartz wool. A feed gas of 1% CO balanced with dry air was passed through the catalysts bed at a flow rate of 12.5 mL/min, corresponding to a gas hourly space velocity (GHSV) of 37,500 mL (h g$_{cat}$)$^{-1}$. The concentrations of CO_2 and CO in the reactor effluent were analyzed using an on-line gas chromatograph (Buck Scientific 910) equipped with a dual molecular sieve/porous polymer column (Alltech CTR1) and a thermal conductivity detector (TCD). The conversion, $C_{CO}(\%)$ was calculated according to Equation 4:

$$C_{CO}(\%) = \frac{[CO]_{inl} - [CO]_{out}}{[CO]_{inl}} \times 100 \qquad \text{(Equation 4)}$$

The steady-state experiment was performed in the same reactor when the CO conversion was below 15.0% to ensure that the reaction was close to under kinetic control as possible. The rate constant, K was determined according to Equation 5:

$$K = \frac{R_t \times C_{co}}{m_{cat}}$$

(Equation 5)

where R_t (mL.s^{-1}) is the total gas flow rate, C_{CO} is the CO conversion (%) at temperature T(K), and m_{cat} is the mass (g) of the catalysts in the reactor. The apparent activation energy, (E_a) was estimated from the slope of the linear plot of ln(K) versus 1000/T according to the non-exponential Arrhenius equation given in Equation 6:

$$\ln(K) = \ln(A) - \frac{E_a}{R}\left(\frac{1}{T}\right)$$

(Equation 6)

where K (s^{-1}) and A (s^{-1}) represent the rate constant and pre-exponential factor, respectively; E$_a$ (kJ mol^{-1}) is the apparent activation energy, R is the gas constant, 8.314 J mol^{-1} K^{-1}; and T(K) is the kelvin temperature.

QUANTIFICATION AND STATISTICAL ANALYSIS

Data were analyzed using OriginPro 2017 (OriginLab Cor., Northampton, Massachusetts, USA).